Parameterization of Convective Momentum Transport in Highly Baroclinic Conditions

VANDA GRUBIŠIĆ* AND MITCHELL W. MONCRIEFF

National Center for Atmospheric Research,+ Boulder, Colorado

(Manuscript received 28 January 1999, in final form 14 October 1999)

ABSTRACT

The organization of convection by vertical shear strongly affects the transport of horizontal momentum, yet the concept of organization has received little attention in convective parameterization. Here the focus is on open-cellular convection in cold-air outbreaks under strongly baroclinic conditions that occur to the rear of midlatitude cyclones. The principles derived herein are envisaged to apply to baroclinic advection at large in similar shear flows.

Open-cellular convection, forced by surface fluxes of sensible and latent heat and organized by unidirectional shear, is simulated using a three-dimensional cloud-resolving numerical model. The effects of the in-cloud pressure field, organization, and shear on momentum transport are quantified for the simulated clouds. A simple analytic model of blocked overturning provides dynamical insight into downgradient momentum transport by the simulated three-dimensional cumulonimbus ensemble. The overturning circulation having vorticity of the same sign as the ambient shear maintains the far-field flow, while the blocking effect decelerates in-cloud momentum. The combined effect is to maintain the mean flow somewhat below its undisturbed value.

The numerical results and analytic predictions are used to evaluate and interpret two parameterization schemes for convective momentum transport used in operational global weather prediction and climate models at the U.K. Meteorological Office and the European Centre for Medium-Range Weather Forecasts. Finally, the authors comment on how the downgradient momentum transport by three-dimensional cumulus convection contrasts with momentum-mixing concepts as well as countergradient momentum transport by two-dimensional squall lines.

1. Introduction

Convection over the ocean in cold-air outbreaks behind midlatitude cyclones exhibits various kinds of organization corresponding to the spatial variation of shear, surface fluxes, and the large-scale divergence of temperature and moisture. Downstream of the polar ice sheet, in the descending equatorward branch of the large-scale slope convection that characterizes a mature cyclone, there occurs a diversity of organization ranging from shear-parallel convection bands, open- and closed-cellular convection, to stratocumulus and fields of cumulonimbus and rainbands that occur in the neighborhood of the cold front. This structural diversity is illustrated in a cold-air outbreak over the Greenland Sea–Norwegian Sea in Fig. 1.

Similar kinds of organization occur over the northern Atlantic and nothern Pacific and extensively over the Southern Hemisphere oceans. This type of convection is also associated with cold outflow from the Siberian anticyclone during winter and early spring over the Sea of Japan, the East China Sea, the South China Sea, and eastern regions of the Pacific. Often referred to as ''cold surges,'' these outbreaks sometimes extend well into tropical regions and organize convection on a wide range of scales. Similar behavior is found over the eastern Atlantic during the cold season when outflow from the American continent encounters the Gulf Stream (Konrad 1998) and also over the Great Lakes. Although cold-air outbreak convection affects huge areas of the world's oceans, it has received scant attention compared to marine stratocumulus associated with ocean upwelling located to the west of continents.

The most intense surface heat fluxes (order 1000 W m^{-2}) on earth occur in polar outbreaks. The attendant cooling is large enough to drive penetrative convection within the ocean and affect the deep oceanic circulation and the climate system on timescales of centuries (Marshall and Schott 1999). Convective momentum transport affects short temporal scales as well. For instance, in midlatitudes, the curl of the surface wind stress drives ocean currents, while the momentum flux divergence within the atmosphere can influence the life cycle and

* Current affiliation: Desert Research Institute, Reno, Nevada.

+ The National Center for Atmospheric Research is sponsored by the National Science Foundation.

Corresponding author address: Dr. Vanda Grubišić, DRI/DAS, 2215 Raggio Pkwy., Reno, NV 89512-1095.
E-mail: grubisic@dri.edu

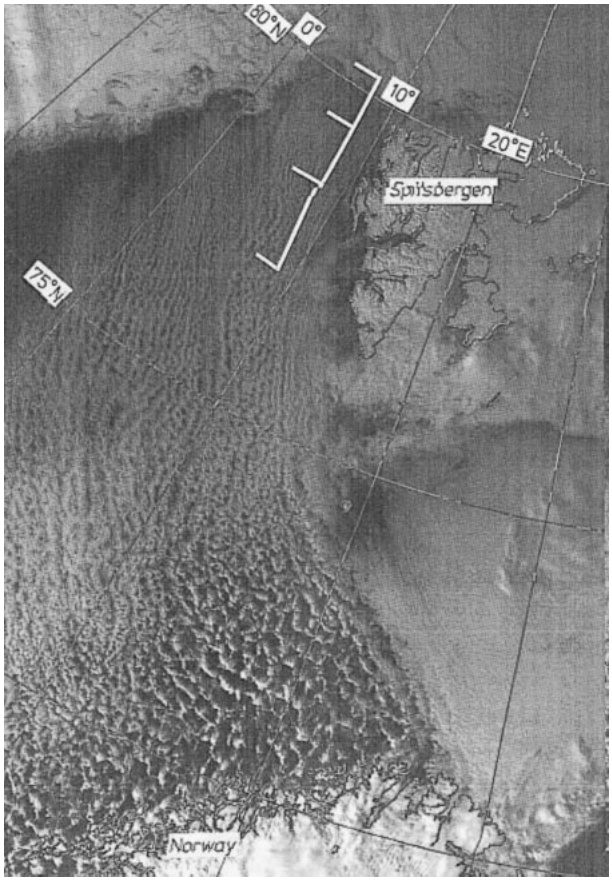

FIG. 1. National Oceanic and Atmospheric Administration infrared satellite image at 1249 UTC 25 Mar 1993 showing a cold-air outbreak off the ice edge near Spitsbergen. The flight pattern on that day from ARKTIS 1993 experiment is marked with white lines (after Brümmer 1999).

tracks of midlatitude cyclonic storms. Although convective momentum transport parameterization affects the accuracy of weather forecast models and is a factor in climate models (Gregory et al. 1997; Gregory 1997), no fundamental explanation is available. Cognizant of these issues, we search for a rigorous basis for momentum transport in cold-air outbreaks in terms of dynamical mechanisms to facilitate development of physically based parameterizations. In view of the above examples, the principles investigated in the context of cold-air outbreaks are envisaged to be relevant to strongly baroclinic conditions at large.

Several attempts have been made to parameterize convective momentum transport. Schneider and Lindzen (1976) assumed that in-cloud horizontal momentum is conserved, which is valid only if the horizontal pressure gradient is negligible. Using observations, Shapiro and Stevens (1980) and Flatau and Stevens (1987) included the pressure gradient in a parameterization scheme. The momentum transport parameterization based on Tiedtke (1989, hereafter T89) accounts for the pressure gradient by increasing the lateral entrainment rate in an empirical way. Guided by observational analyses of mesoscale convective systems, Wu and Yanai (1994) represented the pressure gradient using a linearized approximation of the diagnostic pressure equation. Kershaw and Gregory (1997, hereafter KG) and Gregory et al. (1997, hereafter GKI) derived an empirical relationship for the pressure gradient by employing a cloud-resolving model (CRM).

Recognizing the distinction from squall lines, we examine momentum transport by convection organized into open-cellular patterns. We employ finescale numerical simulations and an analytic model designed to reduce the numerical results to first principles. In the next section we describe numerical simulations of open-cellular convection in an idealized cold-air outbreak, a case originally presented in KG, and analyze the results. In section 3, using the simulation results, we evaluate two mass flux-based parameterizations implemented in global models [U.K. Meteorological Office Unified Model and the European Centre for Medium-Range Weather Forecasts (ECMWF) medium-range weather forecasting model]. An idealized dynamical model presented in section 4 explicates the physical assumptions underlying the above two schemes and provides a simple transport formulation. Finally, in section 5 conclusions are drawn and comments made regarding downgradient transport, countergradient transport, and mixing of momentum.

2. Numerical simulations

a. Cloud-resolving model and experimental design

The cloud-resolving model (CRM), whose Eulerian variant is used in this study, is described in Smolarkiewicz and Margolin (1997). The prognostic variables are the three velocity components (u, v, w); potential temperature θ; water substance mixing ratios q_v, q_c, and q_r (vapor, cloud water, and rain water, respectively); and the turbulent kinetic energy on which the subgrid-scale turbulence model is based (Schumann 1991). We represent moist processes by a bulk parameterization (Kessler 1969; Grabowski and Smolarkiewicz 1996) and disregard the Coriolis acceleration.

The time integration of the discrete equations employs a regular unstaggered rectangular Cartesian mesh. Resolved-scale variables are treated implicitly, whereas subgrid-scale terms and slow phase-change tendencies, such as rain formation and evaporation, are treated explicitly. The elliptic equation for pressure, arising from the anelastic mass conservation constraint, is solved subject to appropriate boundary conditions using the generalized conjugate-residual approach (Smolarkiewicz and Margolin 1994; Smolarkiewicz et al. 1997). Simulations were carried out on a 64-processor CRAY T3D using a massively parallel version of the code (Anderson et al. 1997).

Simulations were initialized with the horizontally ho-

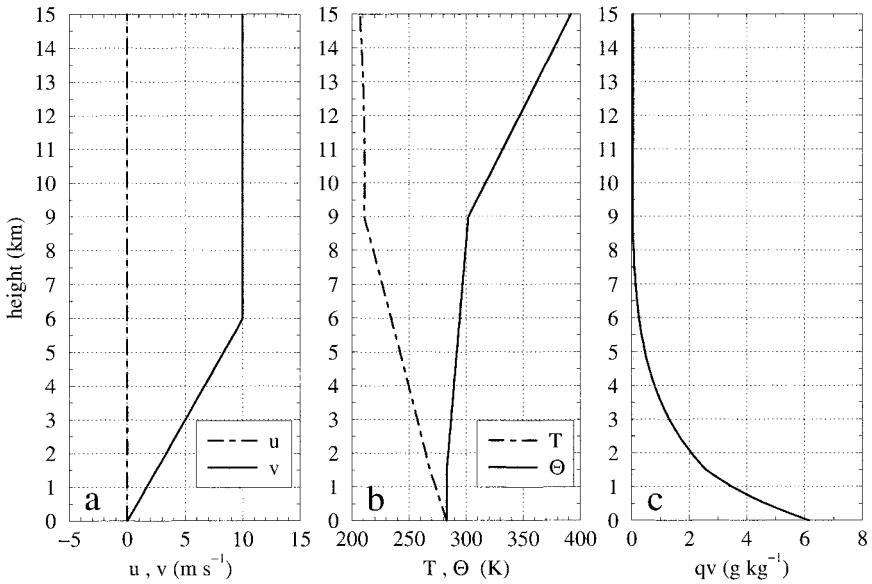

FIG. 2. Initial vertical profiles of (a) horizontal velocity components, (b) temperature and potential temperature, and (c) water vapor mixing ratio for the control simulation of an idealized late-stage midlatitude cold-air outbreak.

mogeneous profiles shown in Fig. 2. The u and w components of velocity and the microphysical variables were initially zero, and the v component is an idealized shear flow. Convection was forced by spatially homogeneous and time-invariant surface fluxes of sensible heat (123 W m^{-2}) and latent heat (492 W m^{-2}). Convection was initiated by small-amplitude random perturbations of temperature ($<$0.002 K) and vertical velocity ($<$0.07 m s^{-1}) introduced in the lowest 1350 m of the domain. The initial profiles and the surface fluxes are identical to those in the idealized cold air outbreak case of KG.

The computational domain (50 km $\times$ 50 km $\times$ 15 km) was represented by a grid of 128 $\times$ 128 $\times$ 101 points, yielding horizontal and vertical grid intervals of $\sim$394 and 150 m, respectively. In order to test the robustness of results with respect to resolution, all experiments were repeated on a grid of 64 $\times$ 64 $\times$ 31 points (horizontal and vertical resolution of $\sim$794 and 500 m). The latter vertical resolution corresponds to that used in the majority of the KG experiments, whereas the larger of the two horizontal grid increments is intermediate to the 500 and 1000 m used by these authors. In order to prevent the undesirable reflection of vertically propagating, convectively generated gravity waves from the rigid upper boundary, the uppermost 5 km of the computational domain consists of a Rayleigh-like absorbing layer. Frictional drag with a drag coefficient $C_d = 0.04$ was imposed at the lower boundary to mimic a no-slip condition. The lateral boundary conditions are periodic.

TABLE 1. List of experiments discussed: control (COA1), lower-resolution (COA2), doubled-shear (COA3), and doubled latent heat flux (COA4) experiments. In all four experiments, sensible heat flux and surface drag coefficients are 123 W m^{-2} and $C_d = 0.04$.

Experiment	Grid		Shear	Latent heat
	Δx (m)	Δz (m)	(m s^{-1}/6 km)	flux (W m^{-2})
COA1	394	150	10	492
COA2	794	500	10	492
COA3	394	150	20	492
COA4	394	150	10	984

The duration of each numerical experiment was 10 h. Convection typically became established in about an hour, and a statistically steady state was attained after a further 3–4 h. Unless otherwise specified, our statistical diagnostics are based on averages over the last 4 h of the control experiment. Besides the lower-resolution experiment, we have performed two more sensitivity tests: one with doubled shear and the other with doubled latent heat flux (Table 1).

b. Analysis of the mean state

The vertical velocity field at a height of 150 m at the end of the second hour of simulation is shown in Fig. 3a. Near the lower boundary, convection is organized into intense, narrow updrafts along the edges and corners of hexagonal cells with weak, broad downdrafts in the middle—a typical open-cellular pattern. During the first few hours the cells broaden and their mean diameter increases from about 7 km at the end of the second hour to more than 30 km between hours 5 and 10. In the mature state, the mean diameter is in qualitative agreement with observations. However, when computer power permits, this result should be tested using a much

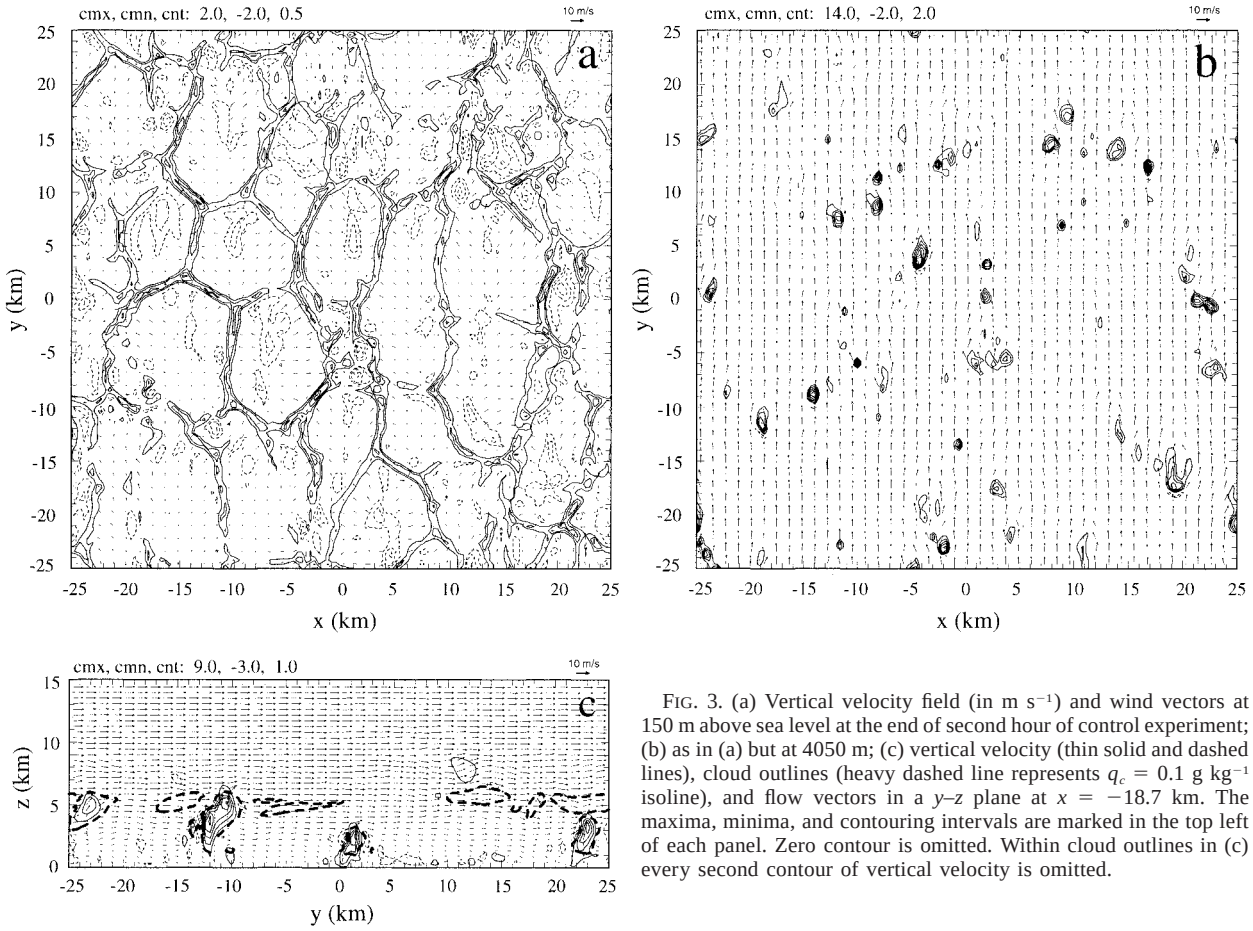

FIG. 3. (a) Vertical velocity field (in m s^{-1}) and wind vectors at 150 m above sea level at the end of second hour of control experiment; (b) as in (a) but at 4050 m; (c) vertical velocity (thin solid and dashed lines), cloud outlines (heavy dashed line represents $q_c = 0.1$ g kg^{-1} isoline), and flow vectors in a y–z plane at $x = -18.7$ km. The maxima, minima, and contouring intervals are marked in the top left of each panel. Zero contour is omitted. Within cloud outlines in (c) every second contour of vertical velocity is omitted.

larger computational domain in case it is an artifact of the periodic lateral boundary conditions.

The cellular pattern is coherent up to a height of about 1400 m. The strong updrafts at the corners of the hexagons (where horizontal convergence is largest) extend toward the middle of the convective layer. The average and maximum vertical velocities in the middle of the convective layer are about 4 and 15 m s^{-1}, respectively. The vertical velocity field at 4 km reveals an ensemble of isolated strong updrafts (in small cumulonimbi) surrounded by broad areas of weak subsidence (Fig. 3b). Figure 3c shows the vertical velocity field and condensate fields (clouds) in various stages in their life cycle in a y–z cross section through the plane at $x = -18.7$ km. Individual updrafts are organized by the environmental shear and tilt slightly downshear (Figs. 4a,b). The in-cloud component of the pressure gradient in the direction of the mean wind is negative (Fig. 4c). Gravity waves generated by convection are evident in the stably stratified layer overlying the convecting layer (Fig. 3c).

In the control experiment, the fraction of grid points occupied by clouds is less than 5% throughout the cloud layer, apart from the outflow (anvil) region between 5 and 7.5 km where it exceeds 50% (Fig. 5a). The maximum value of 95% is attained slightly above 6 km. However, the fractional area occupied by convective updrafts[1] remains nearly constant with height (2.5%). The downdraft fractional area is larger than the updraft area below 4 km and almost constant with height (5%) in the lowest 2 km.

The intensity of convection, measured by the standard deviation of the vertical velocity ($\sqrt{\overline{w^2}}$), is strongest around 5 km (Fig. 5b). Below 7 km the domain-averaged eddy momentum transport is carried mainly by the convective updrafts (Fig. 5c). Above this altitude the transport of momentum by convectively generated gravity waves is significant. The convective momentum transport is downgradient; that is, convection acts to reduce shear and horizontal momentum in the middle of the convective layer. The updraft convective mass flux (Fig. 5d) is nearly constant with height between 1 and 5.5 km; above this height it decreases almost linearly to

[1] For the calculation of the partitioned diagnostics, we have adopted the definitions of KG, where an updraft at a grid point occurs if $w > 1$ m s^{-1} and the condensed water mixing ratio $q_c > 0.1$ g kg^{-1}. A downdraft is defined by $w < 0$ and the precipitating water mixing ratio $q_r > 0.1$ g kg^{-1}.

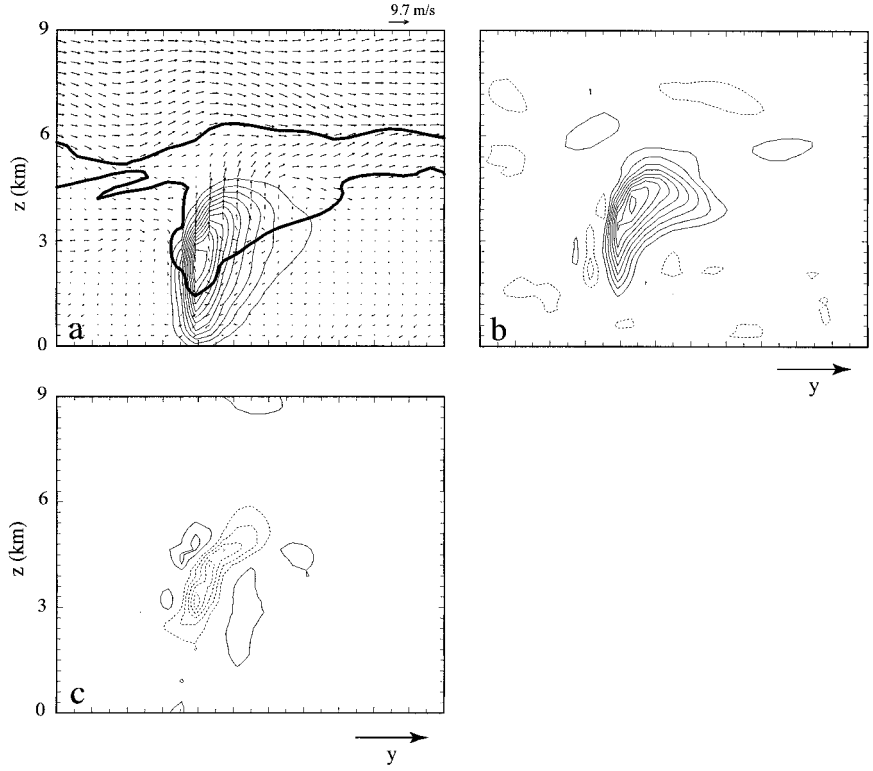

FIG. 4. Vertical section through an individual cloud: (a) cloud outline (thick solid line represents $q_c = 0.1$ g kg^{-1} isoline), rainwater mixing ratio (contouring interval = 0.1 g kg^{-1}), and flow vectors in a system relative coordinates; (b) vertical velocity (contouring interval = 1 m s^{-1}); and (c) pressure gradient (contouring interval = 0.02 kg m^{-2} s^{-2}). Horizontal tick marks are at 0.5 km.

zero at 9 km. The downdraft mass flux peaks at 0.5 km where it reaches half of the updraft maximum.

The pressure gradient force across updrafts and downdrafts is shown in Fig. 6a. The domain average $\overline{v}$ as well as the partitioned averages of the horizontal velocity ($\overline{v}^u$ and $\overline{v}^d$) are shown in Fig. 6b. In agreement with KG, the acceleration by the pressure gradient reduces the difference between in-cloud and environmental momentum ($\overline{v}^u - \overline{v}$) compared to what would occur were in-cloud momentum conserved by air parcels (e.g., Schneider and Lindzen 1976). Within updrafts (downdrafts) air parcels are accelerated (decelerated) by the pressure gradient force proving conclusively that mixing of momentum by convection is not generally valid. If downdrafts originated primarily from the environment, ($\overline{v}^d - \overline{v}$) would most likely be positive despite the effect of the pressure gradient, which would tend to bring $\overline{v}^d$ closer to $\overline{v}$, resulting in negative momentum flux. However, ($\overline{v}^d - \overline{v}$) is negative and the momentum flux carried by downdrafts is positive (cf. Fig. 5c). This implies that the downdrafts mainly recycle updraft air, perhaps by means of an ''up–down'' type of trajectory pattern below 7 km. Above this altitude, in contrast to KG, our results indicate $\overline{v}^d < \overline{v}^u$. A closer inspection of cloud morphology at these levels reveals that isolated overshooting updrafts penetrate the anvil outflow. This overshooting is likely to be an important mechanism for generating the gravity waves seen in the overlying stable layer. The distinction between the two updraft regions, that is, the equilibrium cloud layer and the overshoot region, is confirmed by the updraft vertical velocity profile (Fig. 6c). Consequently, the dynamical model of section 4 will be applied only to the equilibrium cloud layer that includes the anvil outflow.

In order to compare the magnitude of the convectively generated pressure gradient with the other terms of the momentum equation, we have calculated the full momentum budget within updrafts, shown in Fig. 7. Below 5 km, except for the small contribution from the time variability term,[2] the pressure gradient approximately balances three-dimensional advection (Fig. 7a). Above

[2] The time variability term $\sigma^u\overline{\partial v/\partial t}^u = \sigma^u\partial\overline{v}^u/\partial t + (\overline{v}^u - v_b)\partial\sigma^u/\partial t$, where $\overline{(\,)}^u$ represents the average over the updrafts [$\overline{\phi}^u \equiv (1/A_u)\int_{A_u}\phi\,dx\,dy$, where A_u is the total area occupied by updrafts within a grid box area of size A. The equivalent definition holds for downdrafts with the total area A_d.], σ^u ($\equiv A_u/A$) is the updraft fractional coverage, and v_b is the velocity of the updraft interfaces. In the statistically steady state, the first term on the right-hand side is very small. Consequently, the time variability reflects changes of cloud cover dominated by $v_b\partial\sigma^u/\partial t$.

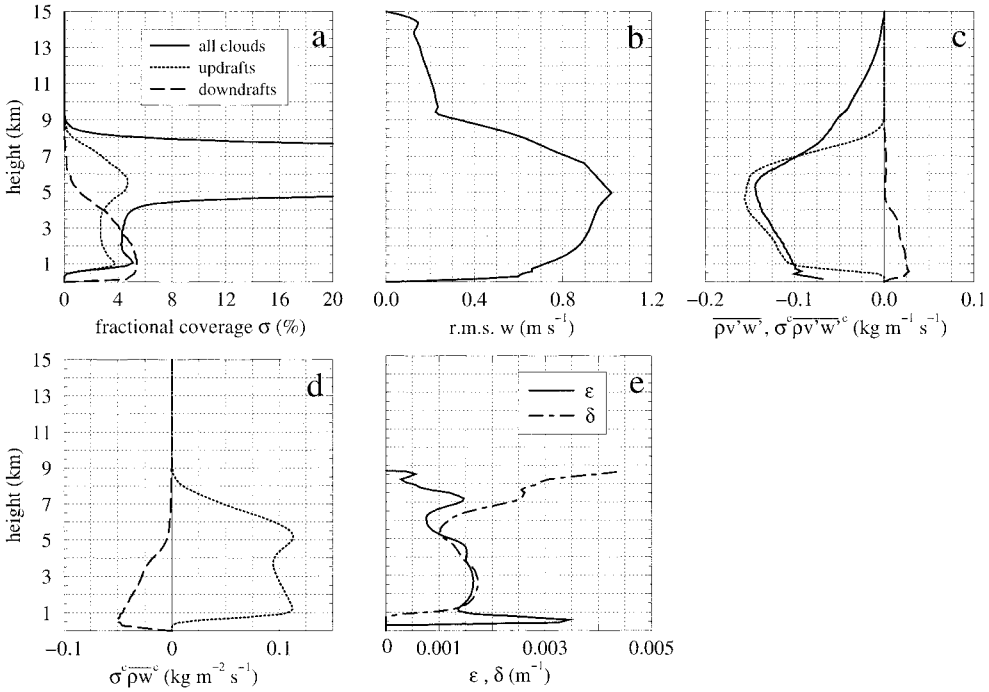

FIG. 5. Ensemble average vertical profiles of (a) fractional cloud coverage, (b) domain average standard deviation of vertical velocity $\sqrt{\overline{w^2}}$, (c) eddy momentum flux, (d) mass flux, and (e) fractional entrainment ϵ and detrainment δ rates for the last 4 h of the control experiment. Except in (a) and (e), thick solid line represents the domain average, whereas dotted and long-dashed lines denote updrafts and downdrafts, respectively.

this altitude, including the anvil outflow and the overshooting updrafts, the time variability term is significantly larger than the pressure gradient term. The subgrid-scale mixing is negligible everywhere, being an order of magnitude smaller than the other terms. Examination of the horizontal and vertical advection terms (Fig. 7b) reveals that the pressure gradient is everywhere almost completely balanced by vertical advection. It also shows that the horizontal advection parallel to the mean wind accounts for the temporal variability—a result consistent with statistically steady precipitating convection traveling at nearly the mean flow velocity. The

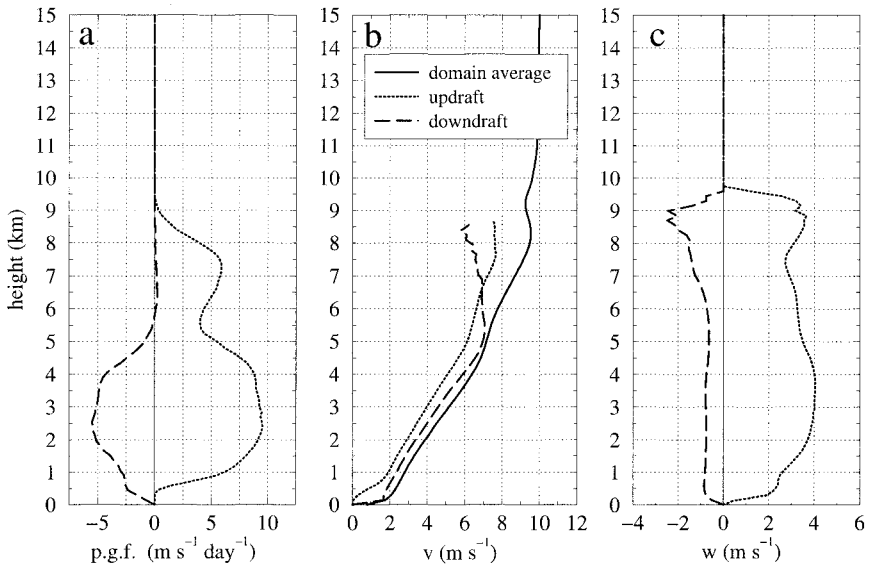

FIG. 6. Ensemble average vertical profiles of (a) horizontal pressure gradient force, (b) horizontal velocity, and (c) vertical velocity. The line patterns used are the same as in Fig. 5.

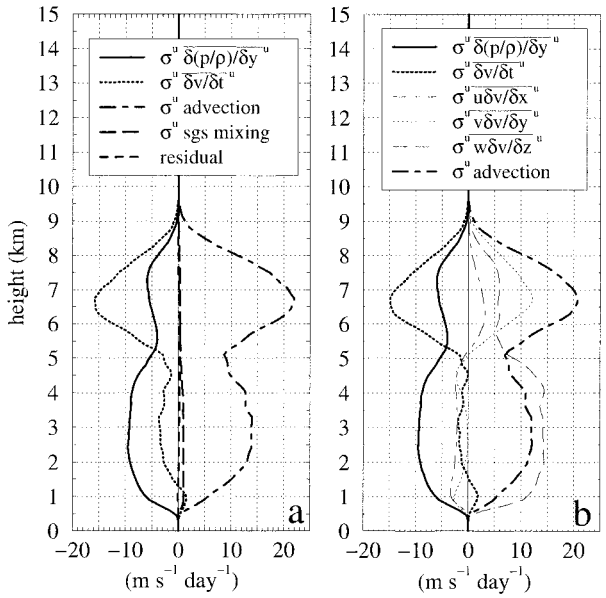

FIG. 7. Updraft momentum budget: (a) exact budget and (b) approximate budget. The exact budget was computed at every time step in a manner consistent with model's numerical algorithms thus yielding full three-dimensional advection. Centered-in-space and forward-in-time differencing was used for the terms of the approximate budget.

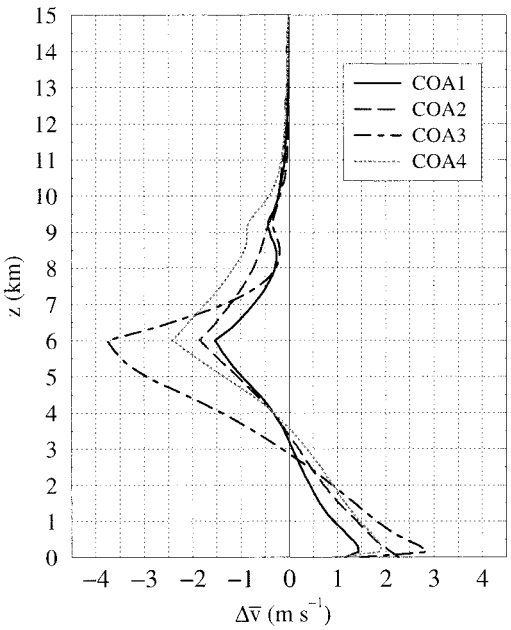

FIG. 8. Total change in the mean velocity profiles $\Delta\overline{v}$ over 10 h of simulation for experiments from Table 1.

contribution of advection perpendicular to the mean wind is small, showing that the transports are approximately two-dimensional (i.e., in the y–z plane).

We now summarize the sensitivity experiments. The ensemble-averaged statistics of the lower-resolution experiment reveal a sensitivity to resolution. While most of the averaged statistics change only weakly with resolution, the updraft mass flux in the lower-resolution experiment is about 25% smaller compared to the control experiment, whereas both the updraft and downdraft pressure gradient forces are about halved. Consequently, as in KG, the resulting cloud-environmental velocity difference and the total momentum forcing are larger in the lower-resolution experiment. Since a very high resolution experiment was not performed, we cannot conclusively say our results converge with increasing resolution, but we anticipate our highest-resolution simulations are reasonably accurate. However, our sensitivity is larger than that reported by Brown (1999a), who shows that many ensemble-averaged statistics of shallow-cumulus convection are comparatively insensitive to resolution.

For the remainder of the sensitivity experiments we found that the doubled shear leads to cumulonimbi with more extensive anvils resulting in 100% cloud cover around 6 km. Also, the momentum flux and the pressure gradient force in the doubled-shear experiment are about double those in the control experiment, whereas the mass flux remains almost unchanged. In the doubled latent heat flux experiment, the clouds reach 1 km higher. The updraft and downdraft cloud fraction, as well as the mass flux and the intensity of convection, are double that in the control experiment. The momentum flux is 50% larger, while the pressure gradients are about twice as strong. As a summary of sensitivity experiments, Fig. 8 shows the total change in the mean velocity profile ($\Delta\overline{v}$) over the 10 h of simulation for all the experiments reported here. For the most part, our results are in good agreement with KG.

3. Evaluation of parameterized quantities

a. Entrainment and detrainment

The convective mass flux is defined as $M^c = \sigma^c\rho\overline{w}^c$, where $\overline{(\,)}^c$ represents averages over convective updrafts or downdrafts whose fractional area σ^c is assumed to be small compared to the grid area. The mass continuity equation averaged horizontally over the convective area (say, updraft) is

$$\frac{\partial M^u}{\partial z} = E - D, \tag{1}$$

where E and D are entrainment and detrainment rates, respectively. It is usual to define a fractional entrainment rate $\epsilon = E/M^u$ and a fractional detrainment rate $\delta = D/M^u$, in which case $1/M^u$ is an integrating factor for (1). It is typically assumed that convection can be represented as an entraining plume (Squires and Turner 1962); however, the values of ϵ and δ used in various convective parameterizations span a large range and are not necessarily consistent with those of Squires and Turner.

As part of the evaluation of the T89 scheme operative

in the ECMWF forecasting system, we have computed the entrainment (E) and detrainment rates (D) for the ensemble of updrafts using the budget equations for scalar variables. Figure 5e shows the fractional rates ϵ and δ. In the middle of the cloud layer, entrainment and detrainment rates are about equal, which is consistent with the mass flux being approximately constant with height. The fractional rates we obtain in this deep convection case are $\epsilon \approx \delta \approx 1.5 \times 10^{-3}$ m^{-1}, which is the same order of magnitude as the rates determined for shallow convection (cf. Brown 1999b). These rates are also an order of magnitude larger than the turbulent entrainment and detrainment rates assumed in deep-convection parameterizations (T89; Gregory and Rowntree 1990). Our results indicate that the fractional rates depend on neither the strength of shear nor the latent heat flux. However, for the lower-resolution experiment we find somewhat larger values of $\epsilon \approx \delta \approx 2 \times 10^{-3}$ m^{-1}.

b. Pressure gradient

The following approximate equation stems from the Reynolds averaging–based mass-flux approach to the parameterization of convective momentum transport,

$$\left(\frac{\partial(\rho\overline{v})}{\partial t}\right)_{\text{conv}} = -\frac{\partial}{\partial z}(\rho\overline{v'w'}) \cong \frac{\partial}{\partial z}[M^c(\overline{v} - \overline{v}^c)], \quad (2)$$

where the $\overline{(\,)}$ denotes an average over a grid box of a large-scale model or an entire domain of a cloud-resolving model, and primes denote departures from domain averages, that is, $v' = v - \overline{v}$. The domain-average eddy momentum flux is approximated by eddy momentum fluxes within updrafts and downdrafts[3] expressed as the product of the convective mass flux and the difference between the in-cloud horizontal momentum and the domain-average momentum.

Since the resolved-scale (mean) momentum $\overline{v}$ is a predicted variable in a large-scale model, in order to close the parameterization, profiles of the cloud mass flux M^c and the in-cloud wind field $\overline{v}^c$ need to be specified. The vertical variation of the latter quantity can be obtained by averaging the horizontal momentum equation over a grid box. In steady state this gives

$$\frac{\partial(\rho\sigma^c\overline{vw}^c)}{\partial z} = E\overline{v} - D\overline{v}^c - \sigma^c\overline{\frac{\partial p}{\partial y}}^c, \quad (3)$$

where entrainment/detrainment (E/D) parameterization is used to represent the horizontal advection and the cloud-interface mixing terms. Applying the mass-flux approximation to $\rho\sigma^c\overline{vw}^c \approx M^c\overline{v}^c$ and substituting (1) for the height variation of mass flux results in

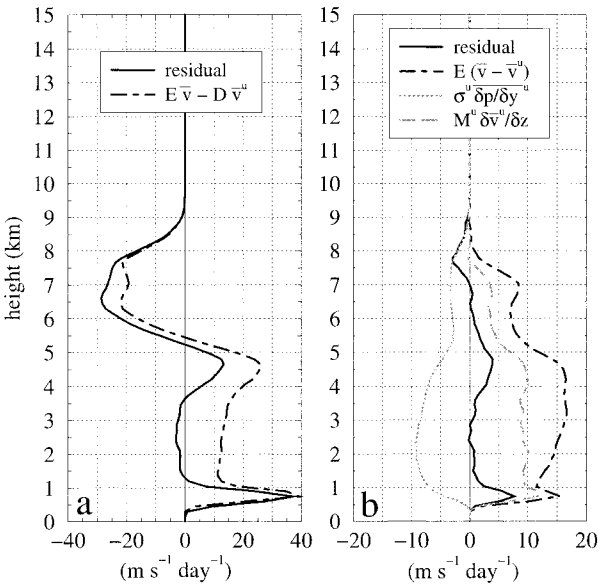

FIG. 9. Horizontal advection and cloud interfacial mixing terms for cloud updrafts computed as (i) residuals and (ii) employing the entrainment/detrainment parameterization in Eqs. (3) and (4) [panels (a) and (b)]. Residuals are equal to (a) $\partial(\rho\sigma^u\overline{vw}^u)/\partial z + \sigma^u\overline{\partial p/\partial y}^u$, (b) $M^u\partial\overline{v}^u/\partial z + \sigma^u\overline{\partial p/\partial y}^u$.

$$M^c\frac{\partial\overline{v}^c}{\partial z} = E(\overline{v} - \overline{v}^c) - \sigma^c\overline{\frac{\partial p}{\partial y}}^c. \quad (4)$$

Thus, determination of $\overline{v}^c$ using (4) requires an approximation of the in-cloud pressure gradients. Before discussing the parameterizations of this term, we focus first on the entrainment and detrainment terms in (3) and (4). Figures 9a,b show the horizontal advection and mixing terms for the updrafts computed as residuals in Eqs. (3) and (4), respectively, and the E/D parameterizations. While the parameterization captures the general shape of the vertical variation of horizontal advection and mixing terms, in particular near the cloud base and in the anvil region (Fig. 9a), it overestimates the magnitude of these terms, especially in the lower portion of the cloud layer where horizontal advection is almost zero. This is also evident in Figure 9b, which further reveals that the vertical profile of in-cloud velocity is strongly controlled by the pressure gradient. The E/D parameterization behaves in the same manner in all four experiments from Table 1; that is, it exaggerates the importance of advection and cloud interfacial mixing throughout most of the cloud layer.

In KG and GKI the convectively generated pressure gradient is parameterized as

$$-\sigma^c\overline{\frac{\partial p}{\partial y}}^c = CM^c\frac{\partial\overline{v}}{\partial z}, \quad (5)$$

where the empirical constant ($C = 0.7$) was evaluated from their numerical simulations of convection in cold-air outbreaks.

As implemented in the ECMWF global model, the

[3] Based on the partitioning $\overline{v'w'} = \sigma^u\overline{v'w'}^u + \sigma^d\overline{v'w'}^d + (1 - \sigma^u - \sigma^d)\overline{v'w'}^e$ in the mass-flux approximation, both updraft and downdraft contributions enter (2), whereas the contribution from the environment is usually neglected.

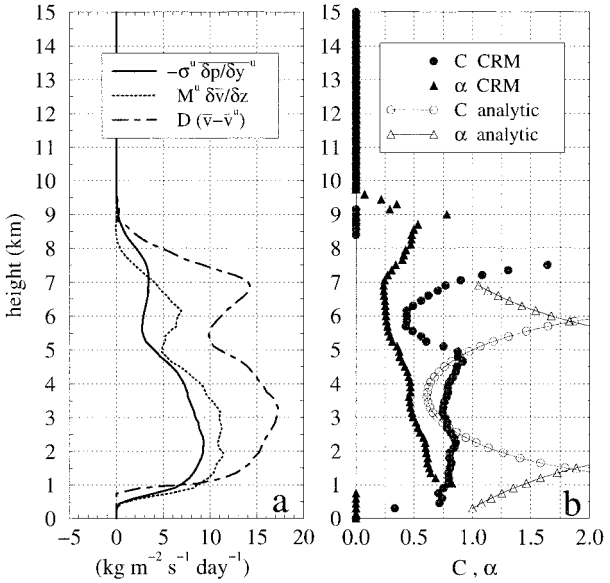

FIG. 10. (a) Pressure gradient force and the two parameterization terms [cf. (5) and (6)] averaged over the last 4 h of the control experiment. (b) Profiles of C and α computed from the CRM results. Open symbols in (b) represent analytic predictions for C and α based on a simple two-dimensional steady-state cloud model of section 4.

pressure gradient in the T89 scheme is approximated as an enhanced entrainment and detrainment which, according to Gregory (1997), translates into the following approximation:

$$-\sigma^c\overline{\frac{\partial p}{\partial y}}^c = \alpha\delta M^c(\bar{v} - \bar{v}^c), \tag{6}$$

where α is an empirical constant. Values used by the ECMWF are $\alpha = 2$ (or 3 if $\epsilon = 0$) for deep convection, and $\alpha = 0$ (or 1 if $\epsilon = 0$) for shallow convection.

We now evaluate the above two pressure gradient approximations using the cloud-resolving model results. Figure 10a shows the two terms on the right-hand side of (5) and (6) computed from the averaged diagnostics by setting C and α equal to unity. The pressure gradient term is also shown for reference. Profiles of C and α, determined as the ratio of corresponding terms in (5) and (6), are shown in Fig. 10b. Throughout the equilibrium cloud layer, between 0.3 and 7 km, the value of C varies between 0.5 and 1.0 with the majority of points clustered near 0.75. Similar results are obtained for the doubled-shear and latent heat flux sensitivity experiments. The corresponding value computed from the lower-resolution diagnostics reveals more variation with height and a mean value closer to 0.5. Overall, the range of values is close to 0.7, the value estimated by GKI based on their numerical experiments.

The results also indicate $\alpha \approx 0.25$–0.5, which is an order of magnitude smaller than the value used for deep convection in the ECMWF scheme. Further inspection of (6) shows that this parameterization depends not only on the assumed value of α but also on the fractional rates ϵ and δ, namely, $\epsilon_{\text{ECMWF}} = \delta_{\text{ECMWF}} = 1 \times 10^{-4}$ m^{-1} for deep convection. Because the fractional rates derived from our simulations are an order of magnitude larger, it follows that $\alpha_{\text{CRM}} \times \delta_{\text{CRM}} \approx \alpha_{\text{ECMWF}} \times \delta_{\text{ECMWF}}$. In other words, given the same mass fluxes for this case of deep convection, namely, $M^u \sim 0.06$ kg m^{-2} s^{-1} for the ECMWF model (Fig. 1 in Gregory 1997) and $M^u \sim 0.1$ kg m^{-2} s^{-1} from our results (Fig. 5d), the ECMWF parameterization with $\alpha = 2$ (or 3) can produce reasonable results for deep convection (cf. Gregory 1997). The ECMWF scheme therefore produces reasonable results by virtue of a compensation of two errors.

More basically, the success of this scheme depends on the validity of the E/D parameterization of the horizontal advection and mixing terms. The ECMWF scheme is relatively successful in this case because the parameterized advection (albeit incorrectly) mimics the vertical variation of the convective pressure gradient (cf. Fig. 9b). However, this is probably not a general result but rather one that depends on convective organization. Indeed, Brown (1999b) documents a poor performance of the ECMWF parameterization for a case of shallow convection.

4. Analytic model

A turbulent entraining plume is a reasonable model to use for parameterizing convection in weakly sheared conditions where small-scale stochastic mixing with the environment (eddy diffusion) is the dominant process. It has long been known that vertical shear has a fundamental effect on convection by organizing the airflow into quasi-steady structures (Ludlam 1980). This concept was quantified in the steady-state nonlinear models of Moncrieff (1981) based on the conservation properties of the inviscid Lagrangian equations of motion and thermodynamics. These analytic models represent distinct regimes of organized airflow and accompanying transports that are fundamentally different from turbulent entraining plumes.

A criterion for determining the relative importance of turbulent mixing and organized flow was established by Moncrieff (1997, section 2.2 therein), measured in terms of a nondimensional number

$$\mathcal{D} = \frac{\dfrac{K_e}{VL}\left(\dfrac{L}{H}\right)^2}{\dfrac{\Delta p}{\rho V^2}}, \tag{7}$$

where Δp is the horizontal pressure change across the cloud system, V is an advective velocity scaling, L and H are characteristic horizontal and vertical scales, K_e is the eddy diffusion of momentum, and K_e/VL is an eddy Reynolds number. Because the momentum budget in Fig. 7 shows turbulent mixing is negligible within simulated clouds, $\mathcal{D}$ is very small and, therefore, the con-

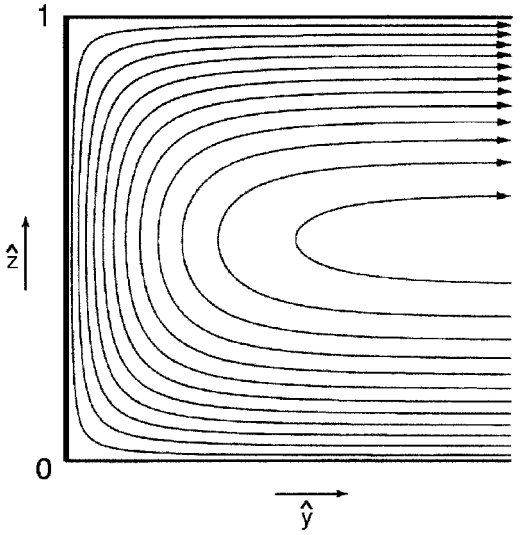

FIG. 11. Schematic illustration of the asymmetric steady, two-dimensional inviscid flow in the constant environmental shear.

vective organization can legitimately be cast in terms of inviscid dynamics.

We develop a variant of the Moncrieff (1981) steering-level regime of convective overturning in constant shear appropriate to the convection simulated herein. This is necessary because the original steering-level model tilts downshear and generates a countergradient transport[4] of momentum (Moncrieff 1978), and the classical model of Moncrieff (1981), which consists of two antisymmetric updraft circulations, does not transport momentum (because the local flux at an arbitrary point in one overturning branch is canceled by the flux of equal magnitude but opposite sign at the image point in the other branch). Note that in Fig. 4 the simulated updrafts tilt slightly downshear, but the accompanying (countergradient) transport does not alter the overall downgradient transport.

The key feature identifying the model adopted here from the classical model is the single, vertically oriented, blocked overturning updraft (Fig. 11). This is an idealization of a simulated three-dimensional cumulonimbus where ambient air flows around the updraft. While three-dimensional transport is neglected in this two-dimensional idealization, the one-sided circulation [a limiting case of the blocked overturning regime of Liu and Moncrieff (1996)] provides the asymmetric pressure gradient responsible for the momentum transport. Kinematically this means that the one-sided (blocked) circulation causes deceleration of the horizontal in-cloud velocity of air parcels, while the vorticity of the overturning updraft, of the same (positive) sign as the ambient shear, maintains the far-field flow. The combined effect of these two mechanisms is to maintain the mean in-cloud momentum at each level at an intensity somewhat less than its domain-averaged value (see Fig. 6b).

In the following analysis, the blocked overturning model will be applied to the equilibrium layer of the ensemble cloud of depth $H = 6.7$ km and aspect ratio $L/H \approx 1$. In the analytic formulation, we assume constant density, constant shear, and neutrally stratified base state, and for convenience, we normalize the relative[5] coordinates and variables according to $\hat{z} \mapsto \hat{z}/H$, $\hat{y} \mapsto \hat{y}/H$, $(\hat{v}, \hat{w}) \mapsto (\hat{v}, \hat{w})/V$, $\hat{\psi} = \psi/(HV)$, and $\hat{p} = p/(\rho V^2)$. The finite-amplitude vorticity perturbation from the undisturbed shear represents potential flow described by solutions of Laplace's equation. In rectangular domain $0 \le \hat{y} \le \hat{L}$, $0 \le \hat{z} \le 1$, where $\hat{L}$ is the aspect ratio, the analytic solution is expressed in terms of the infinite series:

$$\hat{\psi}(\hat{y}, \hat{z}) = \hat{z}(\hat{z} - 1) + \frac{8}{\pi^3} \sum_{n=0}^{\infty} \frac{\sin[(2n + 1)\pi\hat{z}]}{(2n + 1)^3} \times \exp[-(2n + 1)\pi\hat{y}], \tag{8}$$

where the streamfunction satisfies $\hat{v} = \partial\hat{\psi}/\partial\hat{z}$ and $\hat{w} = -\partial\hat{\psi}/\partial\hat{y}$ in the usual way. The series converges so rapidly that the first term is a useful approximation:

$$\hat{\psi}(\hat{y}, \hat{z}) = \hat{z}(\hat{z} - 1) + \frac{8}{\pi^3} \exp(-\pi\hat{y}) \sin\pi\hat{z}; \tag{9}$$

$$\hat{v}(\hat{y}, \hat{z}) = 2\hat{z} - 1 + \frac{8}{\pi^2} \exp(-\pi\hat{y}) \cos\pi\hat{z}; \quad \text{and} \tag{10}$$

$$\hat{w}(\hat{y}, \hat{z}) = \frac{8}{\pi^2} \exp(-\pi\hat{y}) \sin\pi\hat{z}. \tag{11}$$

At the left-hand boundary at $\hat{y} = 0$ the horizontal velocity is zero in the full series solution and approximately zero in the truncated series. Therefore, the average in-cloud horizontal momentum is less than the inflow (environmental) momentum, and the momentum flux is downgradient.

a. Physical basis of pressure gradient approximations

Evoking the model defined in the preceding section, we now establish the physical basis of the GKI and T89 approximations of the convectively generated horizontal

[4] In classic terms "countergradient transport" refers to a negative momentum transport coefficient, but in more generality, it is a mechanism by which the mean flow is accelerated by the action of subgrid-scale transport. Because of the integral constraint on momentum flux, this may not occur throughout the convecting layer but rather in discrete layers (Moncrieff 1992, section 7c and Fig. 12 therein).

[5] A simple coordinate transformation applies between the fixed Eulerian coordinates (x, y, z) and the relative coordinates of the analytic model $(\hat{x}, \hat{y}, \hat{z})$, i.e., $(x, y - v_{SL}t, z) \mapsto (\hat{x}, \hat{y}, \hat{z})$ yielding $(u, v - v_{SL}, w) \mapsto (\hat{u}, \hat{v}, \hat{w})$, where v_{SL} is the steering-level velocity.

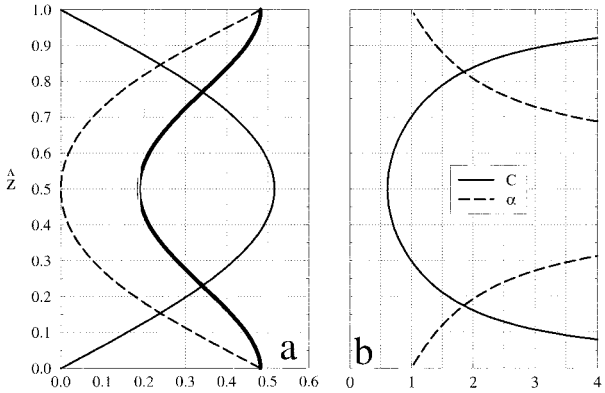

FIG. 12. (a) Height dependence of the horizontally averaged terms of (13). A thick, black solid line represents the pressure gradient force. The horizontal advection term ($\Delta\hat{v}^2$) is displayed with a black dashed line. The vertical advection term ($\hat{L}\overline{\hat{w}\partial\hat{v}/\partial\hat{z}}$) and the mass-flux approximation of this term ($\hat{L}\overline{\hat{w}}\,\partial\overline{\hat{v}}/\partial\hat{z}$) are displayed with gray and black solid lines, respectively; (b) functions C and α as defined by (16) and (18).

pressure gradient and suggest how they could be combined to give a more general parameterization. The steady-state horizontal pressure gradient is balanced by the total advection of momentum

$$-\frac{\partial\hat{p}}{\partial\hat{y}} = \left(\hat{v}\frac{\partial\hat{v}}{\partial\hat{y}} + \hat{w}\frac{\partial\hat{v}}{\partial\hat{z}}\right), \tag{12}$$

where the relatively small term $\hat{u}\partial\hat{v}/\partial\hat{x}$ is neglected. Recall the steady assumption refers to a frame of reference fixed to the moving system; that is, the *relative* flow is steady. Integrating over the horizontal distance $\hat{L}$, and using the identity $\int(\,)\,d\hat{y} = \hat{L}\overline{(\,)}$,

$$-\hat{L}\overline{\frac{\partial\hat{p}}{\partial\hat{y}}} = \Delta\hat{v}^2 + \hat{L}\overline{\hat{w}\frac{\partial\hat{v}}{\partial\hat{z}}}, \tag{13}$$

where $\hat{v}$ is the total flow, and $\Delta(\,) \equiv \frac{1}{2}[(\,)_{\hat{L}} - (\,)_0]$.

The pressure gradient can be calculated from the analytic values of $(\hat{v}, \hat{w})$. On substituting (10) and (11) in (12) and averaging over distance $\hat{L} \approx 1$, we obtain

$$-\hat{L}\overline{\frac{\partial\hat{p}}{\partial\hat{y}}} = \frac{8}{\pi^2}\left[(1-2\hat{z})\cos\pi\hat{z} + \frac{2}{\pi}\sin\pi\hat{z} - \frac{4}{\pi^2}\right]. \tag{14}$$

Figure 12a shows the height dependence of the horizontally averaged momentum equation terms: the pressure gradient force (14), the horizontal advection ($\Delta\hat{v}^2$), and vertical advection ($L\overline{\hat{w}\partial\hat{v}/\partial\hat{z}}$). The mass-flux approximation to the last term ($L\overline{\hat{w}}\,\partial\overline{\hat{v}}/\partial\hat{z}$) is also shown for reference. The physical distinction between the horizontal and vertical advection implies their height dependence will be very different. This is a key point since the T89 and the GKI convective momentum transport parameterizations, as shown below, are, respectively, based on one and only one of these contributions.

In GKI the left-hand side of (13) was approximated as

$$-\hat{L}\overline{\frac{\partial\hat{p}}{\partial\hat{y}}} = C\hat{M}^u\frac{\partial\overline{\hat{v}}}{\partial\hat{z}}, \tag{15}$$

where C is an empirical constant determined from the cloud-resolving simulations. Comparing (13) and (15) this mass flux–type approximation is justified provided the following is satisfied. First, in-cloud shear and the (pointwise) mass flux (here $\hat{M}^u \equiv \hat{L}\hat{w}$) are uncorrelated yielding the ''top-hat'' profile for vertical velocity used in mass-flux schemes expressed in terms of an entraining plume model. Second, the horizontal momentum advection is neglected ($\Delta\hat{v}^2 = 0$). In other words, the horizontal pressure gradient is provided solely by the vertical advection of momentum.

The analytic model shows that rather than being a constant, C should be a function of height:

$$C(\hat{z}) = \pi \times \frac{\pi^2(1-2\hat{z})\cos\pi\hat{z} + 2\pi\sin\pi\hat{z} - 4}{2\sin\pi\hat{z}(\pi^2 - 4\sin\pi\hat{z})}, \tag{16}$$

which has a minimum value $C_{\min} = \pi/(\pi+2) \approx 0.61$ at $\hat{z} = \frac{1}{2}$ (Fig. 12b). The empirical value proposed by GKI is $C = 0.7$, whereas our CRM results suggest a value closer to 0.75 (cf. Fig. 10). The assumption regarding horizontal advection is valid at the cloud layer midlevel, but its legitimacy deteriorates toward the upper and lower boundaries where C becomes singular. The singularity and the concave shape of $C(\hat{z})$ in Fig. 12b stem from the neglect of the horizontal convergence, which increases from zero at the middle of the cloud to a maximum at the upper and lower boundaries—the value of C must increase accordingly to compensate for this neglected term. In Fig. 10b, the analytic prediction for C is compared to the C profile based on the GKI parameterization. We note that the two C profiles agree reasonably well in the middle of the cloud layer, but the agreement rapidly deteriorates toward the bottom and the top.

Wu and Yanai (1994) used a linearized approximation of the diagnostic pressure equation to determine the horizontal pressure gradient using a cumulus ensemble representation of Arakawa and Schubert (1974), in which each element is an entraining plume. They also assumed that horizontal advection does not contribute to the pressure gradient. It follows that their expression for the horizontal pressure gradient has the same form as that used by GKI [cf. Eq. (16) of Wu and Yanai and Eq. (15) herein], whose mass flux has a sinusoidal variation akin to our series solution. As Wu and Yanai point out, the calculation of γ (the counterpart of C) requires explicit knowledge of convection dynamics. In their study, a linearized analysis provides γ in terms of a ratio of the characteristic wavenumbers, whereas herein the pressure gradient is provided by the analytic model.

Inspection of (13) shows that, converse to GKI, the method of T89 neglects the vertical advection of momentum; that is, the pressure gradient is represented solely by horizontal advection approximated as an en-

hanced entrainment and detrainment [cf. Eq. (6)]. It follows that

$$-\hat{L}\overline{\frac{\partial \hat{p}}{\partial \hat{y}}} = \alpha \Delta \hat{v}^2. \quad (17)$$

As a corollary to the physical argument made for C, α should vary with height according to

$$\alpha(\hat{z}) = \frac{\pi^2(2\hat{z} - 1)\cos\pi\hat{z} - 2\pi\sin\pi\hat{z} + 4}{\pi^2(2\hat{z} - 1)\cos\pi\hat{z} + 4\cos^2\pi\hat{z}}, \quad (18)$$

where $\alpha = 1$ at the upper and lower boundaries. The profile of α in Fig. 12b stems from the fact that the vertical advection of momentum, a maximum at the midlevel and zero at the boundaries, is neglected. In order to compensate, α must increase toward the midlevel where it is unbounded.

Recall that the empirical value used in the ECMWF model for deep convection is $\alpha = 2$ and that the value based on our numerically simulated data varies from 0.25 to 0.5 throughout the cloud layer. For reference, in Fig. 10b we have also included the analytic form for α. Following from the discussion in section 3b, the large discrepancy between the analytic and the simulation-based α is due to the overestimation of the horizontal advection and cloud interfacial mixing terms by the E/D parameterization at and below the midcloud level where these terms are nearly zero (cf. Fig. 9).

Following from the above discussion based on (12), a more general representation of the convectively generated pressure gradient should take account of both vertical and horizontal advection terms. Thus,

$$-\sigma^c\overline{\frac{\partial p}{\partial y}}^c = C_1(z)M^c\frac{\partial \overline{v}}{\partial z} + C_2(z)\delta M^c(\overline{v} - \overline{v}^c), \quad (19)$$

assuming the last term is a reasonable approximation to horizontal advection. Functions $C_1(z)$ and $C_2(z)$, perhaps both constant, could be determined from numerical simulation results.

b. Analytic representation of ensemble properties

In order to show the analytic model captures the salient dynamical properties of the numerically simulated cloud ensemble, we have computed the individual terms of (13) averaged over the updrafts. Since the steady-state analytic model is cast in system-relative coordinates, the horizontal advection term is given by $\hat{v}\partial\hat{v}/\partial\hat{y} = (H/V^2)(v\partial v/\partial y - v_{SL}\partial v/\partial y)$, where v_{SL} is the steering-level velocity of the cloud ensemble. By relating the horizontal average of (10) to the domain-average velocity of the numerically simulated cloud ensemble, it follows that during the last 4 h of the control experiment $v_{SL} = 5.5$ m s^{-1}. This is approximately the initial mean flow velocity near the midcloud level at $z = 3.65$ km.

In Fig. 13 we show the pressure gradient term, the vertical and horizontal advection terms, and their ratios

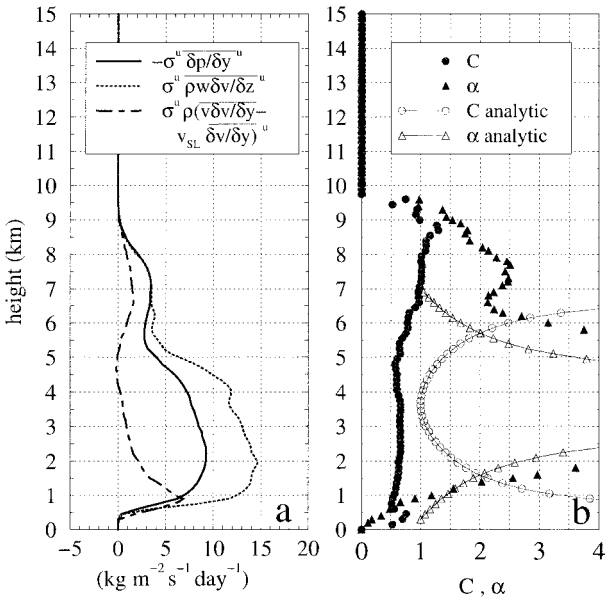

FIG. 13. As in Fig. 10 but for the exact terms of the momentum equation.

calculated using the approach adopted in section 3b with the parameterization terms. This analysis reinforces the point that the pressure gradient mimics vertical advection throughout most of the cloud layer (cf. Figs. 7 and 9b). The ratio of these two terms is approximately equal to a half below 5 km and is close to unity in the anvil region and within the overshooting updrafts. The corresponding analytic ratio for organized convection of vertical extent 0.3–7 km, also shown in Fig. 13b, starts from unity at the midcloud level and gradually becomes unbounded toward the top and bottom of the cloud layer. As predicted by the analytic model, the organized inflow and outflow due to horizontal advection contributes significantly to the pressure gradient term only in the top and bottom portions of the cloud layer. Consequently, the ratio of the latter two terms reflects the height dependence exhibited by the analytic model.

Based on the preceding analysis, as well as the analysis of momentum budget and entrainment and detrainment, we conclude that the vertical advection of momentum is the more accurate approximation of the in-cloud pressure gradient. For this reason, one can say the GKI parameterization is preferable to the T89 method, which is based solely on the horizontal advection.

In the following, we quantify the analytic transport dependence on the asymmetry of the blocked overturning updraft. Referring to (10) and (11), it is worthwhile to note that the overturning updraft has constant vorticity equal to the environmental shear. Also, the horizontal velocity, while decelerated in the updraft region, asymptotes to the undisturbed environment for $\hat{y} \gg L$. Consequently, the downgradient momentum flux and the tendency to maintain shear are a hallmark of this regime of convection.

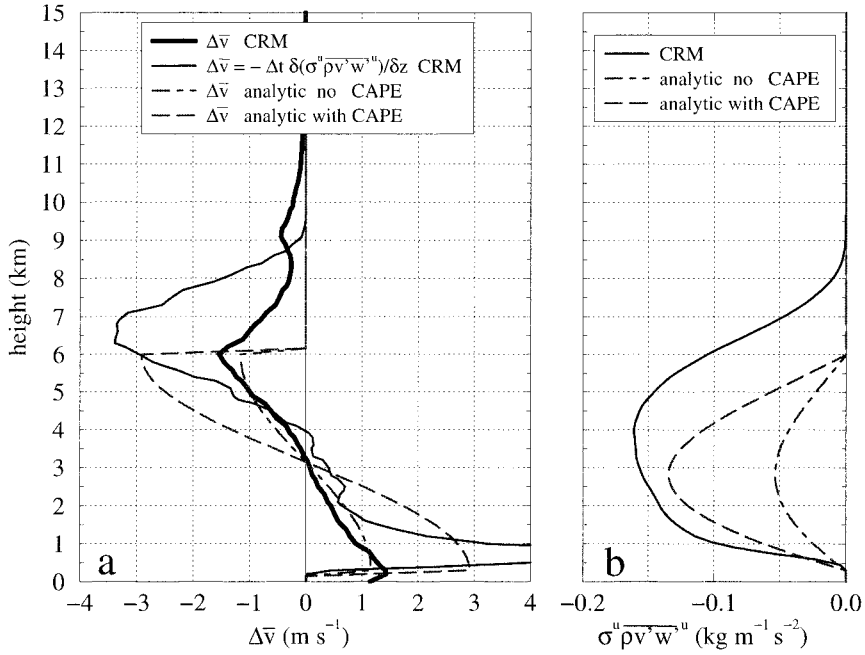

FIG. 14. Vertical profiles of (a) total convective momentum forcing and (b) updraft momentum flux. The CRM derived results are for the entire 10 h of the control simulation.

Because the analytic model has a near-field solution, we can explicitly calculate the convective momentum tendency $\Delta\overline{\hat{v}}/\Delta\hat{t}$ and, by employing (2), the momentum transport $\overline{\hat{v}'\hat{w}'}^u$ by an overturning updraft. Recognizing that (10) represents the total flow—that is, the mean flow component ($2\hat{z} - 1$) plus a nonlinear perturbation—the tendency, over a discrete time interval Δt, is

$$\frac{\Delta\overline{\hat{v}}}{\Delta\hat{t}} = \left(\frac{2}{\pi}\right)^3 \cos\pi\hat{z}. \tag{20}$$

The vertical profile of the momentum transport by updrafts is then

$$\rho\overline{v'w'}^u = -\frac{VH\rho}{\pi\Delta t}\left(\frac{2}{\pi}\right)^3 \sin\pi\hat{z}. \tag{21}$$

The cosine dependence of the tendency and the negative-definite sinusoidal form of the momentum flux are consistent with the numerical simulation analysis (Fig. 14). Together they justify the downgradient transport property of the blocked overturning updraft model of blocked flow around three-dimensional updrafts. The time interval Δt used to obtain the results shown in Figs. 14a,b is the entire 10 h of the simulation. For this longer averaging period, the equilibrium cloud layer extends only up to 6 km ($H = 5.7$ km), and the steering-level velocity is $v_{SL} = 5$ m s^{-1}.

The momentum flux provided by the analytic model is of correct sign and shape, but its amplitude is smaller than the numerically simulated results. We note that the analytic model represents neutral overturning in which kinetic energy is provided solely by the pressure gradient, whereas in the simulations at midlevels the conversion of convective available potential energy (CAPE) into kinetic energy is dominant. The effects of CAPE and the pressure field are estimated in the appendix. As shown in Fig. 14b, the inclusion of CAPE leads to a better agreement of the momentum flux profiles within the equilibrium cloud layer.

Finally, we reiterate that the analytic blocked overturning model applies only to the equilibrium state of the convecting layer. The momentum tendency near 6 km is associated with the overshooting updrafts between 6 and 8.5 km. These different regions are depicted in Fig. 15.

5. Conclusions

We evaluated two momentum parameterization schemes operational in global models (GKI and T89) using the cloud-resolving numerical simulations of open-cellular convection in an idealized midlatitude cold-air outbreak and the blocked overturning model. In spite of its simplicity, this two-dimensional analytic model captures the salient features of the three-dimensional numerical realizations. This success is due to (i) the blocked overturning updraft having the same vorticity as the ambient shear, and (ii) the cross-stream flow perturbations in unidirectional mean flow being second order, meaning the momentum transport is approximately two-dimensional.

The GKI and T89 schemes are based on the traditional

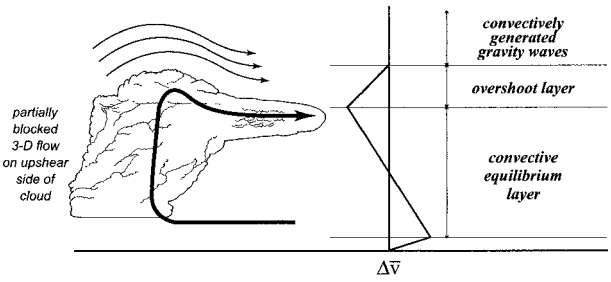

FIG. 15. Summary diagram depicting features of simulated clouds and convective momentum forcing by open-cellular convection under highly baroclinic conditions in unidirectional shear. (An idealization based on Figs. 4a and 8.)

mass-flux approximation to the eddy Reynolds stress where the formidable problem is the representation of the convectively generated pressure gradient. We established that the GKI scheme approximates the pressure gradient in terms of the vertical advection of momentum. The analytic model shows this approximation to be accurate at midlevels, but the accuracy deteriorates toward the upper and lower boundaries. For the numerically simulated convection, however, this approximation is evidently valid throughout almost the entire updraft depth. Conversely, the T89 scheme approximates the pressure gradient solely by the horizontal advection of momentum by way of enhanced entrainment and detrainment. In the analytic model, this is reasonable at upper and lower levels but not at midlevels where the vertical advection dominates. In the simulations, while the entrainment/detrainment parameterization of horizontal advection and cloud-interfacial mixing overestimates these terms, it mimics the vertical variation of the pressure gradient. On physical grounds, the representation of the pressure gradients by means of the vertical advection of momentum (GKI) is the better approximation.

The downgradient momentum transport associated with the blocked overturning updraft contrasts with the countergradient transport by squall lines, a property quantified in dynamical models (Moncrieff 1981, 1992) and identified in observations (LeMone 1983; Wu and Yanai 1994). Countergradient transport by *two-dimensional squall lines* is due to the upshear tilt of relative airflow. This tilt occurs if the sign of the ambient flow reverses with height (jetlike profiles) or if the shear is strong in low levels but weak aloft. The blocked overturning model is a simple representation of the salient aspects of *three-dimensional cumulonimbus* convection simulated herein. The mechanism was explained in terms of the pressure gradient or, alternatively, in terms of a blocked vertically oriented updraft having vorticity of the same sign as the mean flow shear.

GKI showed that the entraining plume works in practice when empirically tuned. In principle, however, for reasons already described it is not truly appropriate for organized convection. Ambient shear controls different regimes of convective momentum transport, yet shear is not part of any existing parameterization scheme. This situation must be rectified if momentum transports are to be properly represented in large-scale models.

Acknowledgments. The research reported herein has been performed during the lead author's affiliation with the Clouds in Climate Program at NCAR. V. G. acknowledges partial support from the Desert Research Institute in final stages of this work. We thank David Gregory for helpful discussions and all our reviewers for valuable comments and suggestions.

APPENDIX

Analytic Representation of the Effect of CAPE

In the overturning updraft model of section 4, the vertical velocity has a maximum at the left-hand boundary at the point $(\hat{y}, \hat{z}) = (0, \hat{z}_*)$, where $\hat{z}_*$ is the height of the steering level. In case of neutral overturning,[A1] $\hat{z}_{0*} = \frac{1}{2}$, that is, $z_{0*} = H/2$. In the buoyant updraft, the steering level is shifted toward the upper boundary so that $H/2 < z_{1*} < H$. The vertical velocity maxima can be determined by applying Bernoulli's theorem along the lower-boundary streamline from inflow at $(\hat{L}, 0)$ to $(0, \hat{z}_*)$. By noting that the pressure perturbation vanishes $\forall \hat{z}$ at $\hat{y} = \hat{L}$,

$$\frac{1}{2}w_*^2 = \frac{1}{2}V^2 + \int_0^{z_*} g\frac{\delta\theta}{\theta}\,dz - \frac{\delta p_*}{\rho}, \qquad \text{(A1)}$$

in dimensional form. If for simplicity we assume that the parcel lapse rate (γ) and the static stability (B) are constant, the integral on the right-hand side is equal to $g(\gamma - B)z_*^2/2$. The pressure perturbation $\delta p_*/\rho$ can be estimated from the steady-state momentum equation integrated along $z = z_*$ to yield $\delta p_*/\rho \approx V^2/4$. Thus,

$$\frac{1}{2}w_*^2 = \frac{1}{4}V^2 + \text{CAPE}\left(\frac{z_*}{H}\right)^2, \qquad \text{(A2)}$$

where $\text{CAPE} \equiv g(\gamma - B)H^2/2$. In the neutral updraft, $w_{0*}^2 = V_0^2/2$. Assuming further the same vertical shear in both models, that is, $V_1/z_{1*} = 2V_0/H$, and defining $\Delta V \equiv V_H - V_0$, it follows that $V_1 = \Delta V(z_{1*}/H)$. By substituting the solution of Moncrieff and Green (1972) for z_{1*}/H, the ratio of the buoyant solution to the neutral one is

$$\frac{w_{1*}}{w_{0*}} = 2\frac{1 + \sqrt{1 + 4R}}{3 + \sqrt{1 + 4R}}\sqrt{1 + 2R}, \qquad \text{(A3)}$$

where $R \equiv 2\,\text{CAPE}/(\Delta V)^2$ is the convective Richardson number. It follows that the intensity of buoyant ascent

[A1] In the following, subscripts 0 and 1 denote the neutral and buoyant models, respectively.

compared to neutral overturning is a function of the convective Richardson number.

Based on the ten-hour averaged statistics from the control simulations, CAPE $\approx$ 30 J kg^{-1} and ΔU = 6.5 m s^{-1}. Thus, R = 1.4 and (w_{1*}/w_{0*}) = 2.5. The momentum flux and the total convective momentum forcing shown in Figs. 14c,d have been multiplied by $(w_{1*}/w_{0*})^2$ to approximate the effect of CAPE.

REFERENCES

Anderson, W. D., V. Grubišić, and P. K. Smolarkiewicz, 1997: Performance of a massively parallel 3D non-hydrostatic atmospheric fluid model. *Proc. Int. Conf. on Parallel and Distributed Processing Techniques and Applications PDPTA '97*, Las Vegas, NV, Computer Science Research, Education, and Applications Tech, 645–651.

Arakawa, A., and W. H. Schubert, 1974: Interaction of a cumulus ensemble with the large-scale environment, Part I. *J. Atmos. Sci.*, **31,** 674–701.

Brown, A. R., 1999a: The sensitivity of large-eddy simulations of shallow cumulus convection to resolution and subgrid model. *Quart. J. Roy. Meteor. Soc.,* **125,** 469–482.

——, 1999b: Large-eddy simulation and parametrization of the effects of shear on shallow cumulus convection. *Bound.-Layer Meteor.,* **91,** 65–80.

Brümmer, B., 1999: Roll and cell convection in wintertime Artic cold-air outbreaks. *J. Atmos. Sci.,* **56,** 2613–2636.

Flatau, M., and D. E. Stevens, 1987: The effect of horizontal pressure gradients on the momentum transport in tropical convective lines. Part I: The results of the convective parameterization. *J. Atmos. Sci.,* **44,** 2074–2087.

Grabowski, W. W., and P. K. Smolarkiewicz, 1996: Two-time-level semi-Lagrangian modeling of precipitating clouds. *Mon. Wea. Rev.,* **124,** 487–497.

Gregory, D., 1997: Parametrization of convective momentum transports in the ECMWF model: Evaluation using cloud resolving models and impact upon model climate. *Proc. New Insights and Approaches to Convective Parametrization, ECMWF Workshop,* Reading, UK, ECMWF, 208–227.

——, and P. R. Rowntree, 1990: A mass flux convection scheme with representation of cloud ensemble characteristics and stability dependent closure. *Mon. Wea. Rev.,* **118,** 1483–1506.

——, R. Kershaw, and P. M. Inness, 1997: Parametrization of momentum transport by convection. II: Tests in single-column and general circulation models. *Quart. J. Roy. Meteor. Soc.,* **123,** 1153–1183.

Kershaw, R., and D. Gregory, 1997: Parametrization of momentum transport by convection. I: Theory and cloud modelling results. *Quart. J. Roy. Meteor. Soc.,* **123,** 1133–1151.

Kessler, E., 1969: *On the Distribution and Continuity of Water Substance in Atmospheric Circulations. Meteor. Monogr.,* No. 32, Amer. Meteor. Soc., 84 pp.

Konrad, C. E., II, 1998: Persistent planetary scale circulation patterns and their relationship with cold air outbreak activity over the eastern United States. *Int. J. Climatol.,* **18,** 1209–1221.

LeMone, M. A., 1983: Momentum transport by a line of cumulonimbus. *J. Atmos. Sci.,* **40,** 1815–1834.

Liu, C., and M. W. Moncrieff, 1996: A numerical study of the effects of ambient flow and shear on density currents. *Mon. Wea. Rev.,* **124,** 2282–2303.

Ludlam, F. H., 1980: *Clouds and Storms.* The Pennsylvania State University Press, 405 pp.

Marshall, J., and F. Schott, 1999: Open-ocean convection: Observations, theory, and models. *Rev. Geophys.,* **37,** 1–64.

Moncrieff, M. W., 1978: The dynamical structure of two-dimensional steady convection in constant vertical shear. *Quart. J. Roy. Meteor. Soc.,* **104,** 543–567.

——, 1981: A theory of organised steady convection and its transport properties. *Quart. J. Roy. Meteor. Soc.,* **107,** 29–50.

——, 1992: Organized convective systems: Archetypal dynamical models, mass and momentum flux theory, and parametrization. *Quart. J. Roy. Meteor. Soc.,* **118,** 819–850.

——, 1997: Momentum transport by organized convection. *The Physics and Parametrization of Moist Atmospheric Convection,* R. K. Smith, Ed., NATO ASI Series, Vol. 505, Kluwer Academic, 231–253.

——, and J. S. A. Green, 1972: The propagation and transfer properties of steady convective overturning in shear. *Quart. J. Roy. Meteor. Soc.,* **98,** 336–352.

Schneider, E. K., and R. S. Lindzen, 1976: A discussion of the parameterization of momentum exchange by cumulus convection. *J. Geophys. Res.,* **81,** 3158–3160.

Schumann, U., 1991: Subgrid length-scales for large-eddy simulation of stratified turbulence. *Theor. Comput. Fluid Dyn.,* **2,** 279–290.

Shapiro, L. J., and D. E. Stevens, 1980: Parameterization of convective effects on the momentum and vorticity budgets of synoptic-scale Atlantic tropical waves. *Mon. Wea. Rev.,* **108,** 1816–1826.

Smolarkiewicz, P. K., and L. G. Margolin, 1994: Variational solver for elliptic problems in atmospheric flows. *Appl. Math. Comput. Sci.,* **4,** 527–551.

——, and ——, 1997: On forward-in-time differencing for fluids: An Eulerian/semi-Lagrangian non-hydrostatic model for stratified flows. *Atmos.–Ocean,* **35** (special issue), 127–152.

——, V. Grubišić, and L. G. Margolin, 1997: On forward-in-time differencing for fluids: Stopping criteria for iterative solutions of anelastic pressure equations. *Mon. Wea. Rev.,* **125,** 647–654.

Squires, P., and J. S. Turner, 1962: An entraining jet model for cumulonimbus updraughts. *Tellus,* **14,** 422–434.

Tiedtke, M., 1989: A comprehensive mass flux scheme for cumulus parameterization in large-scale models. *Mon. Wea. Rev.,* **117,** 1779–1800.

Wu, X., and M. Yanai, 1994: Effect of vertical wind shear on the cumulus transport of momentum: Observations and parameterization. *J. Atmos. Sci.,* **51,** 1640–1660.